Results in Engineering 32 (2026) 112676

Contents lists available at ScienceDirect

Results in Engineering

journal homepage: www.sciencedirect.com/journal/results-in-engineering

Research paper

A comprehensive study of thermal effects in novel laser photovoltaic converters for high power applications

Javier F. Lozano [a,*], Natalia Seoane [a], Julián G. Fernández [a], Enrique Comesaña [b], Antonio García-Loureiro [a]

[a] *Centro Singular de Investigación en Tecnoloxías Intelixentes (CiTiUS), Departament of Electrónica e Computación, Universidade de Santiago de Compostela, Rúa de Jenaro de la Fuente, s/n, Santiago de Compostela, 15782, Spain*

[b] *Escola Politécnica Superior de Enxeñaría, Campus Terra, Universidade de Santiago de Compostela, Rúa de Lope Gómez de Marzoa, s/n, Lugo, 27002, Spain*

ARTICLE INFO

Keywords:
High power laser transmission
Laser power converters
Silicon carbide
Thermal management

ABSTRACT

The power that high-power laser transmission technology can deliver is currently limited by series resistance losses and the heat generated within the photovoltaic receiver, both of which degrade performance. Several strategies have been proposed to overcome series resistance, yet the thermal aspect remains underexplored, with most studies focusing on performance assessment through temperature control. In this work, we evaluate the temperature in a recently proposed state-of-the-art 4H-SiC photovoltaic receiver using a Technology Computer-Aided Design (TCAD) methodology that incorporates all relevant heat sources and phenomena. All temperature-dependent models are calibrated against experimental data. Several laser power density values and heat sink scenarios are considered. For ultra-high laser power densities (100–500 W/cm^2), two contact resistance values are also examined, as series resistance losses play a major role in performance at these power levels. The results show that for low-to-medium laser power densities (1–10 W/cm^2), 4H-SiC devices can achieve conversion efficiencies exceeding 70% even with conventional thermal management solutions, with heat sink performance causing only a 0.3% and 2.3% efficiency degradation at 1 and 10 W/cm^2, respectively. At 100 W/cm^2, the device achieves a 75.1% efficiency with $h = 10^5$ W/m^2·K and $\rho_c = 10^{-5}$ Ω/cm^2. At 500 W/cm^2, an efficiency of 70.8% is achieved under optimal thermal and contact conditions, while increasing contact resistivity by one order of magnitude results in a 10.4% efficiency degradation, highlighting the importance of thermal management and low contact resistivity at ultra-high power densities. These results also enable a comprehensive thermal management analysis of photovoltaic receivers.

1. Introduction

Among the various approaches to far-field wireless power transfer, high-power laser transmission (HPLT) stands out as particularly compelling [1]. By delivering energy through a laser beam to a photovoltaic receiver, this technique inherently provides galvanic isolation and eliminates electromagnetic interference [2]. The transmission medium can be tailored to the application: optical fiber links remove the need for copper cabling, mitigating spark hazards in ATEX (from the french ATmosphères EXplosives) classified environments [3], whereas free-space propagation lends itself to aerospace platforms. The resulting versatility has spurred interest across a broad spectrum of use cases, from combined power-and-data links [4,5] to remotely powered antennas [6], unmanned aerial vehicles [7], and orbital assets [8,9].

The III-V compounds, particularly GaAs, have long dominated the landscape of the HPLT photovoltaic receivers [10], commonly referred to as laser power converters (LPCs). Under room-temperature conditions, conversion efficiencies above 60% have been demonstrated [11], with a record 68.9% at 11.4 W cm^{-2}. However, as incident power densities increase, efficiency degradation driven by ohmic losses becomes increasingly pronounced [12], spurring the development of strategies [13], and novel device architectures [14–18].

A parallel strategy to improve LPC performance is focused on wide-band gap materials [19–21]. The higher photon energy associated with these materials translates into increased output voltage and reduced current, thereby mitigating series resistance losses while simultaneously lowering intrinsic entropic losses. Within this context, silicon carbide (SiC) emerges as a compelling alternative to conventional

* Corresponding author.
E-mail address: javierfernandez.lozano@usc.es (J. F. Lozano).
URL: https://citius.gal/team/javier-fernandez-lozano (J. F. Lozano)

https://doi.org/10.1016/j.rineng.2026.112676
Received 8 April 2026; Received in revised form 3 August 2026; Accepted 26 August 2026
Available online 30 August 2026

lower-bandgap absorbers such as silicon or gallium arsenide. Over the past two decades, SiC has been extensively developed, finding widespread use in power electronics [22], with the 4H and 6H polytypes emerging as the most widely adopted [23].

Beyond its wide bandgap, SiC offers additional attributes that further enhance its suitability as base material for LPCs. High thermal stability, radiation hardness, and exceptional dielectric strength [24,25] render these polytypes particularly attractive for electronic devices and sensors destined for space applications, environments where conventional materials like Si and GaAs undergo significant degradation [26,27]. The manufacturing processes are also more environmentally benign, employing less toxic agents than GaAs processing, while leveraging established, low-cost silicon fabrication methodologies [28].

These two strategies (the use of novel architectures and wide bandgap materials) are designed to reduce the series resistance losses and enable the transmission of very high laser power densities, which could broaden the range of applications of the technology, powering larger devices and minimizing the size of the receivers. However, at these larger laser power densities, heat dissipation mechanisms become an important issue. Indeed, the increase of the temperature of the device has been pointed out as a key aspect to manage large laser power densities [29]. Most studies of the temperature effect on LPCs usually rely on controlling the device temperature with heaters/cryostats [30–34], while few approaches assess the device temperature depending on the laser power density, mostly by measuring the open-circuit voltage [35] or the electro- and photo- luminescence [36]. Other TCAD studies have shown the dynamics of the LPC recombinations under several temperatures [37]. A deeper understanding of temperature dynamics and thermal management in LPCs is therefore essential. The viability of HPLT technology in high-power applications depends critically on the ability to assess and control the operational temperature, making the study of the material properties and device design features that govern thermal behavior a key research priority.

In this work, we implement a Technology Computer-Aided Design (TCAD) methodology to study and understand heat generation within an LPC. To do so, we employ an optimized 4H-SiC device, which in previous studies has been identified as a strong candidate for efficiently converting high laser powers [38]. All relevant temperature-dependent phenomena are modeled and validated against experimental data. The methodology consists of two stages: a transient simulation in which the device temperature evolves to its steady-state value under zero bias, followed by a steady-state bias sweep to determine the operational temperature at the maximum power point. In addition to a complete thermal analysis, we examine several use cases at different power levels and with different heat sinks, using appropriate thermal convection coefficient values. For ultra-high incident powers, two contact resistivity scenarios are considered. The results broaden the understanding of thermal processes within LPCs and highlight the importance of tailoring thermal management to each specific use case.

2. Simulation methodology

This section shows the simulation framework used in this work. This includes all the TCAD tools, the models and parameters employed to properly account the SiC features, the device structure and the optimization mechanisms employed to find the best set of design parameters.

2.1. TCAD features

In this study, we employ Silvaco [39], a TCAD simulator extensively utilized for modeling various semiconductor devices, including photovoltaic cells. This software has been successfully applied to simulate laser power converters [14], multijunction concentrator solar cells [40], and VEHSA devices [16]. The current density–voltage (J-V) characteristics of the devices are obtained by solving Poisson's equation and the carrier continuity equations within the drift–diffusion framework, which is widely used to model charge transport and electrostatics in semiconductor photovoltaic devices [41].

The Silvaco module Giga [39] allows users to account for lattice heat flow and general thermal environments. This capability is common when simulating power devices, such as floating guard rings, field plates and similar structures. Giga implements Wachutka's thermodynamically rigorous lattice heating model [42], which incorporates Joule heating, thermal effects from carrier generation and recombination, and contributions from the Peltier and Thomson phenomena. The software self-consistently accounts for the temperature dependence of material and transport parameters. Furthermore, it enables the modeling of complex thermal environments through the combined specification of realistic heat-sink structures, thermal impedances, and ambient temperatures. The LASER.ANNEAL model accounts for the heat produced by the optical generation of carriers. This allows to calculate the lattice temperature in transient mode, specifying the duration of the laser pulse. The thermal boundary conditions can be defined in every region of the device, and can be modelled as fixed values, blackbody radiators, heat sinks and thermal capacitances.

The simulation procedure for a given laser power density and heat convection coefficient value is as follows: first, the photogeneration in the device is solved in transient mode, at short circuit current conditions (no bias). Once the temperature is stabilized, we solve the bias. Each bias point of a J-V curve represents a stationary solution, with a stable temperature value associated. With the temperature found at the maximum power point, this process iterates with the updated optical absorption, since this parameter cannot be implemented as a dynamic function of temperature in Silvaco. In the first stage (transient mode), only the LPC is considered in the self-heating process, as the heat sink is treated as a thermal boundary condition at a fixed temperature rather than an explicit simulation region, which would significantly increase the time required to reach thermal stability. This simplification does not affect the subsequent steady-state bias simulations. Since the temperature at the maximum power point is updated at each iteration, the overall procedure accounts self-consistently for both the LPC and the heat sink, converging when the temperature reaches a stable steady-state value.

2.2. Models and parameters

This section shows the temperature-dependent physical models and related parameters of 4H-SiC used in the course of the simulations. All relevant parameter values are fitted to match experimental or DFT generated curves found in literature. The physical models incorporated in the simulation framework are selected based on their direct influence on LPC performance. Specifically, the heat capacity and thermal conductivity govern the thermal dynamics of the device [42], bandgap narrowing and optical absorption determine the photogeneration profile and output voltage [43], and carrier mobility controls carrier transport and recombination [41], all of which exhibit strong temperature dependence in 4H-SiC [44].

The heat capacity, C_p, is modeled as:

$$C_p = \beta_{C_p,1} + \beta_{C_p,2} \cdot T_L + \beta_{C_p,3} \cdot T_L^2 + \frac{\beta_{C_p,4}}{T_L^2} \tag{1}$$

where $\beta_{C_p,1}$, $\beta_{C_p,2}$, $\beta_{C_p,3}$ and $\beta_{C_p,4}$ are fitting coefficients and T_L is the lattice temperature. These parameters are adjusted for the model to follow the DFT heat capacity curve extracted from [45], as seen in Fig. 1 (a).

The thermal conductivity was modelled using an effective phonon-scattering expression inspired by the Callaway framework [46],

$$\kappa(T) = \kappa_\infty + \frac{\beta_{\kappa,1}}{T_L^2} + \frac{\beta_{\kappa,2}}{T_L^3} \tag{2}$$

where κ_∞ represents the saturation thermal conductivity at high lattice temperatures, accounting for residual non-phononic or temperature independent contributions. The T_L^{-2} term captures the dominant

Table 1
Heat capacity and heat conductivity parameters dependent on the temperature. These parameters fit the experimental data from [45,50].

Model	Heat capacity (T)				Heat conductivity (E, T)		
Parameter	$\beta_{C_p,1}$ [J· cm^{-3}·K^{-1}]	$\beta_{C_p,2}$ [J· cm^{-3}·K^{-2}]	$\beta_{C_p,3}$ [J· cm^{-3}·K^{-3}]	$\beta_{C_p,4}$ [J· cm^{-3}·K]	κ_∞ [W·m^{-1}·K^{-1},]	$\beta_{\kappa,1}$ [W·K· m^{-1}]	$\beta_{\kappa,2}$ [W·K^{3}· m^{-1}]
Value	-0.927	$1.349\cdot10^{-2}$	$-1.054\cdot10^{-5}$	$7.823\cdot10^{2}$	-25.433	$1.795\cdot10^{7}$	$-8.554\cdot10^{8}$

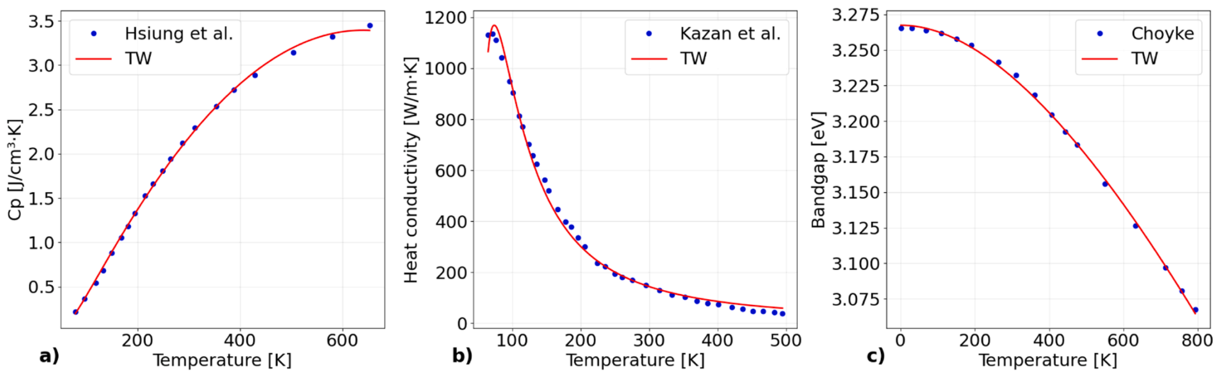

Fig. 1. Validation of heat capacity (a), heat conductivity (b) and bandgap energy (c) implemented models of 4H-SiC for several temperatures. The experimental data (blue dots) is taken from Hsiung et al. [45], Kazan et al. [50] and Choyke [52], respectively. The implemented models in this work (TW) correspond to the red curves. (For interpretation of the references to colour in this figure legend, the reader is referred to the web version of this article.)

phonon-phonon Umklapp scattering mechanism, which governs thermal resistance at intermediate and high lattice temperatures [46,47]. The additional T_L^{-3} contribution is interpreted as an effective higher-order phononic term arising from the coexistence of multiple scattering processes [48,49]. $\beta_{\kappa,1}$ and $\beta_{\kappa,2}$ are fitting coefficients. The presented model enables a robust fit to experimental 4H-SiC data [50] over a wide temperature interval, as shown in Fig. 1b). The heat capacity and heat conductivity fitted parameters are shown in Table 1.

The bandgap energy temperature dependence is modeled following the Varshni expression [51], implemented in Silvaco as:

$$E_G = E_{G,300} + \beta_{EG,1}\cdot\left[\frac{(300\mathrm{K})^2}{(300\mathrm{K})+\beta_{EG,2}} - \frac{T_L^2}{T_L+\beta_{EG,2}}\right] \tag{3}$$

being $E_{G,300}$ the bandgap energy at 300 K and $\beta_{\mathrm{EG},1}$, $\beta_{\mathrm{EG},2}$ are the fitting parameters, which values are shown in Table 2, obtained from fitting the experimental curve from Choyke [52], as seen in Fig. 1c).

The optical absorption also depends on the lattice temperature. A complete study of the absorption coefficient α with dependence on incident photon energy and temperature can be found on Grivickas et al. [53]. The present work uses a purely empirical relation to account for both the photon energy and temperature dependence in a single formula to be implemented in TCAD:

$$\alpha = \beta_{\alpha,1} + \beta_{\alpha,2}\cdot 10^{\left[\frac{E_\gamma+\beta_{\alpha,3}+\beta_{\alpha,4}\cdot T_L}{\beta_{\alpha,5}}\right]} \tag{4}$$

where E_γ is the incident photon energy in electronvolts and $\beta_{\alpha,1}$, $\beta_{\alpha,2}$, $\beta_{\alpha,3}$, $\beta_{\alpha,4}$ and $\beta_{\alpha,5}$ are fitting parameters. Table 2 also shows the values of these parameters that fit the experimental curves from Grivickas et al. [53], as seen in Fig. 2.

The low-field mobility is modeled after the Caughey-Thomas equation, which accounts for the doping density and temperature dependence [54]. The expression, as implemented in Silvaco, is as follows:

$$\mu = \mu_{min}\cdot\left(\frac{T_L}{300K}\right)^{\beta_{\mu,1}} + \frac{\mu_{max}\cdot\left(\frac{T_L}{300K}\right)^{\beta_{\mu,2}} - \mu_{min}\cdot\left(\frac{T_L}{300K}\right)^{\beta_{\mu,1}}}{1+\left[\left(\frac{T_L}{300K}\right)^{\beta_{\mu,3}}\cdot\left(\frac{N}{N_{crit}}\right)^{\beta_{\mu,4}}\right]} \tag{5}$$

where μ_{min}, μ_{max} are the minimum and maximum mobility values, N the doping concentration, $\mathrm{N_{crit}}$ a reference doping value and $\beta_{\mu,1}$, $\beta_{\mu,2}$, $\beta_{\mu,3}$, $\beta_{\mu,4}$ fitting parameters. These parameters, shown in Table 3 were adjusted to follow experimental curves, from Pernot et al. [55] for the

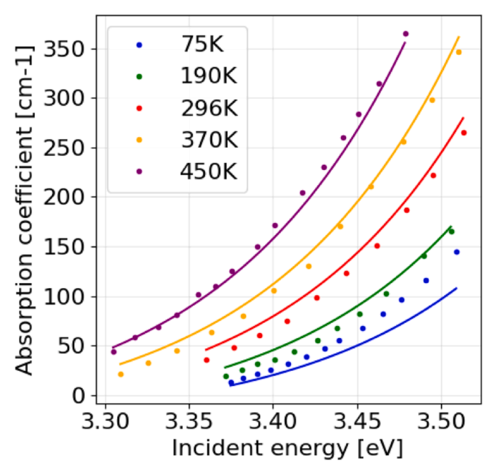

Fig. 2. Validation of the absorption coefficient modeling used in the simulations (solid lines) against experimental data from Grivickas et al. [53] (dots) for several incident photon energies and temperatures.

electron mobility and from Koizumi et al. [56] for the hole mobility for various doping values in each case, as seen in Fig. 3 (left) and Fig. 3 (right), respectively.

The simulations also include the following recombination processes: Shockley–Read–Hall (SRH), which is the main recombination mechanism in indirect bandgap semiconductors [57], and Auger recombination, which affects at high injection levels. The beam-device interaction is modeled with the ray tracing method [39]. An isotropic thermal conductivity model was adopted and fitted to the cross-plane experimental data reported by Kazan et al. [50], which is consistent with the predominantly cross-plane heat flow in the simulated device geometry. Anisotropic thermal transport in 4H-SiC is therefore not considered.

2.3. Device

Fig. 4 shows a scheme of the hLPC structure used in work. The elemental cell of the device employs a four-layer P+/P/N/N+ stack. The optimization of the hLPC device design parameters was performed using a global grid optimizer, since there are many factors that can affect the

Table 2
Bandgap narrowing and optical absorption parameters dependent on the temperature. These parameters fit the experimental data from [52,53].

Model	Bandgap narrowing (T)			Optical absorption (E, T)				
Parameter	$E_{G,300}[eV]$	$\beta_{EG,1}$ [eV/K]	$\beta_{EG,2}$ [K]	$\beta_{\alpha,1}$ [cm^{-1}]	$\beta_{\alpha,2}$ [cm^{-1}]	$\beta_{\alpha,3}$ [eV]	$\beta_{\alpha,4}$ [eV/K]	$\beta_{\alpha,5}$ [eV]
Value	3.231	7.84e-4	1640	-30.54	10.56	-3.26	3.81e-4	0.25

Table 3
Caughey-Thomas mobility parameters that fit the 4H-SiC experimental data, for electrons [55] and holes [56].

Parameter	$\mu_{min}[\frac{cm^2}{V\cdot s}]$		$\mu_{max}[\frac{cm^2}{V\cdot s}]$		$N_{crit}[cm^{-3}]$		$\beta_{\mu,1}$		$\beta_{\mu,2}$		$\beta_{\mu,3}$		$\beta_{\mu,4}$	
Carrier type	e^-	h^+	e^-	h^+	e^-	h^+	e^-	h^+	e^-	h^+	e^-	h^+	e^-	h^+
Value	0	0	1026	117	1.72e17	3.25e18	1.93	8.42	-2.74	-3.21	-2.48	-2.97	0.55	0.46

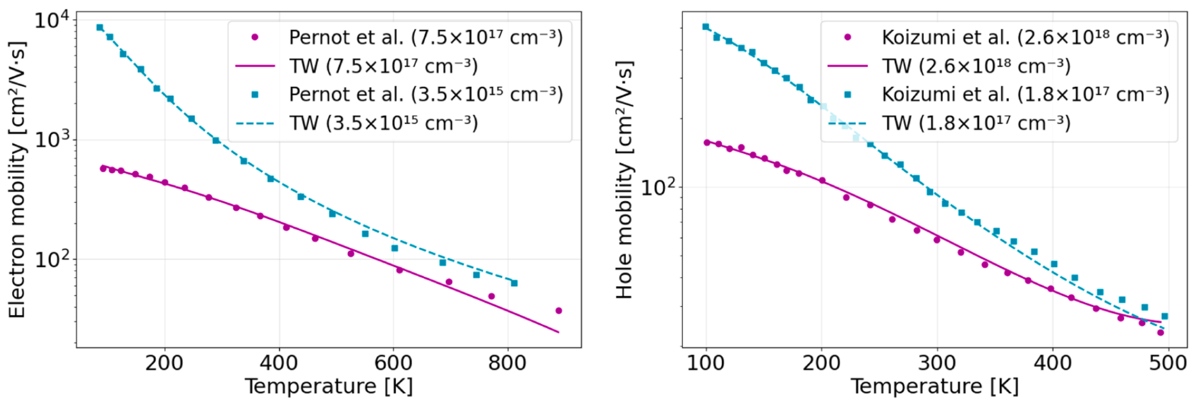

Fig. 3. Validation of Caughey-Thomas mobility parameters that fit the 4H-SiC experimental data at different doping concentrations and temperatures, for electrons [55] (left) and holes [56] (right).

performance of the device. This method consists of defining the minimum, maximum, and step values of all the design parameters (dopings and thicknesses of the layers) and simulating all the possible configurations. The optimum values are shown in Fig. 4. The selected laser wavelength is 355 nm, which is a 7.5% higher than the bandgap energy at 300 K.

To reduce computational effort without affecting the results, the depth is fixed at 1 μm and the width at 10 μm; the latter is justified by the vertical nature of carrier transport and the availability of surface passivation techniques [58]. A total transmittance boundary condition at the illuminated surface emulates an ideal anti-reflective coating, a valid simplification for monochromatic illumination. Given the low absorption coefficients of indirect-bandgap SiC polytypes [59], a reflective back layer is incorporated to enhance optical path length, promoting absorption and photon recycling [60] while preventing excessive device thickness that would increase bulk recombination. Electrical contacts consist of a top cathode covering 3% of the illuminated area and a full bottom anode. The heat sinks are modeled by the heat convection coefficients (h values) applied on the back contact. The initial lattice and heat sink temperatures are set to 298 K.

Fig. 5 (left) shows the mesh of the 4H-SiC LPC. The mesh is refined at the top and bottom contact regions and at the PN junction, where accurate resolution of the electric field and current density is required to correctly capture carrier transport and collection. The remaining regions use a coarser grid, sufficient to resolve the photogeneration profile. The mesh consists of 6046 nodes and 11,756 triangles. Fig. 5 (right) shows a close-up of the top contact region (top), where the local refinement is necessary to accurately capture the sharp gradients in current density near the metal-semiconductor interface, and a zoom of the PN junction (bottom), showing the meshing in the electric field.

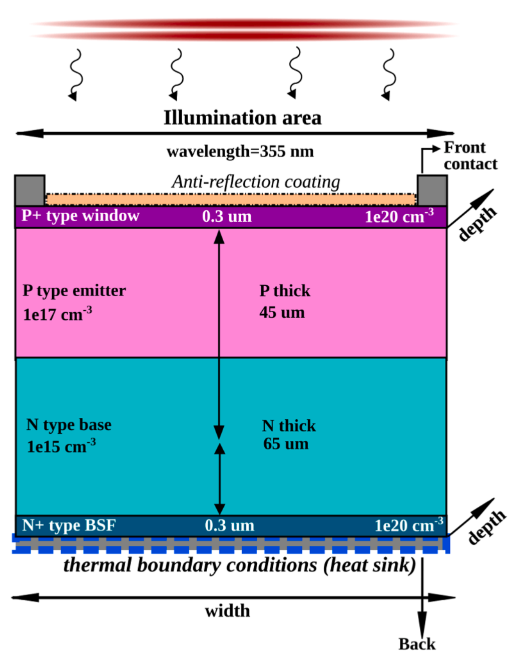

Fig. 4. 2D scheme of the hLPC architecture. The structure of the cell is P+/P/N/N+ doping types. The width and depth dimensions are fixed to 10 and 1 μm, respectively, to save computational costs. The device optimal design parameters are shown in the figure. The heat sink placement, on the bottom contact, is also shown. The initial lattice and heat sink temperature is set to 298 K.

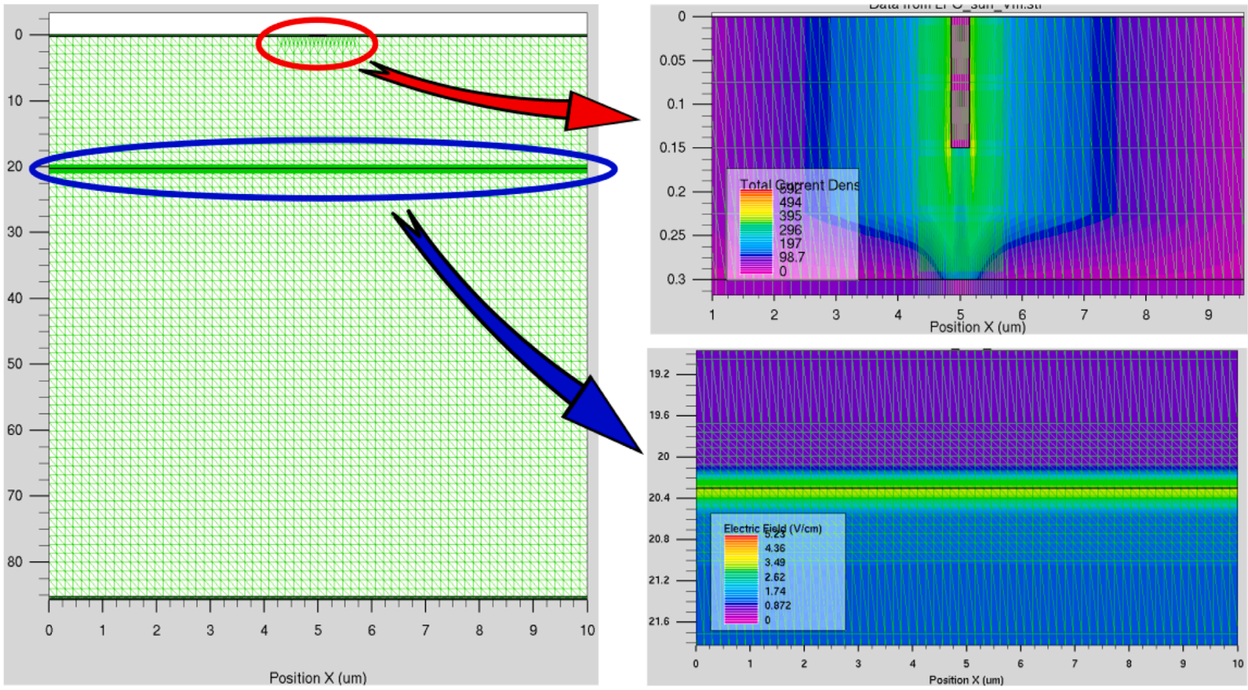

Fig. 5. Mesh of the 4H-SiC LPC (left) and zooms (right) of: the top contact showing the current density (top) and the PN junction showing the electric field (bottom).

The proposed simulation framework enables comprehensive thermal management analysis of LPCs. Efficient thermal management is a key requirement in photovoltaic devices, even more in LPCs due to the amount of power transferred. The performance of the overall thermal management system depends critically on the quality of the thermal interfaces between the device and the heat sink. Microscopic surface roughness, interfacial voids, and imperfect mechanical contact trap low-conductivity air at these interfaces, creating thermal resistance that impedes heat flow and raises the device operating temperature [61]. Thermal interface materials (TIMs) are specifically designed to address this problem by filling interfacial gaps and reducing contact resistance, thereby improving heat transfer between the LPC and the heat sink. However, this methodology does not account for the material and mass of the heat sink, nor the properties of the interface between the heat sink and the LPC. This work focuses on the thermal dynamics of the LPC and the physical mechanisms governing the temperature dependence on the applied bias. For this purpose, the heat sink and its interface with the LPC are treated as a single lumped parameter that determines the final steady-state temperature. The transient temperature evolution presented here accounts only for the LPC itself; in a real system, the transient response will additionally depend on the mass and thermal properties of the heat sink.

3. Results

This section shows the simulation results for the optimized 4H-SiC hLPC at several laser power densities (1, 10, 100 and 500 W/cm^2) considering different heat convection coefficients (250, 2·10^3, 10^4 and 10^5 W/m^2·K). These values represent different approaches, from forced convection of gases through fins [62] (250 W/m^2·K) to a novel Triply Periodic Minimal Surface (TPMS) based Diamond heat sink fabricated from CuCrZr alloy [63] (10^5 W/m^2·K). For the two higher laser power densities (100 and 500 W/cm^2) we considered two contact resistance scenarios: 10^{-5} and 10^{-4} Ω·cm^2 [64], which indicate how ohmic the contact is. For the two lower laser power densities (1 and 10 W/cm^2) we only considered contact resistance of 10^{-5} Ω·cm^2, since the series resistance at these power densities is not as relevant as in the higher ones. To emulate the behavior of a large device, we scaled the series resistance accordingly. We chose the inverted square grid pattern, which has proven to dramatically reduce the series resistance in the field of concentration photovoltaics [65]. We considered the width of the fingers to be 3 μm and a spacing between fingers of 100 μm.

Fig. 6 shows the global device temperature versus the transient time at a laser power density of 100 W/cm^2 for different heat sink convection coefficients: 2·10^3, 10^4 and 10^5 W/m^2·K. The heat sink material is not considered in this simulation, only the LPC. The global device temperature is an average value of the whole device. The time step is 0.02 s for all simulations. For each convection value, the device temperature stabilizes at different times, increasing this time when the h value is lower, since more time is needed to extract the heat. For h = 10^5 W/m^2·K, the device temperature stabilizes at 305.6 K in the first 0.05 s. For h = 10^4 W/m^2·K, the temperature achieves 376.5 K past 0.3 s. For the lower heat convection value, 2·10^3 W/m^2·K, the device temperature increases up to 638.6 K during 1 s of simulation.

Table 4 shows the main figures of merit for the 1 and 10 W/cm^2 laser power densities. These figures of merit are the short circuit current density (J_{SC}), the open circuit voltage (V_{OC}), the voltage at the maximum power point (V_M), the temperature at the maximum power point (T_{VM}) and the efficiency of the device (Eff). Since the temperature of the device increases dramatically near V_{OC} due to the recombination of carriers, the convergence is usually lost in the J-V curves for points past V_M. For that reason, the J-V curves need to be extrapolated to find V_{OC}, using a cubic spline method. The V_{OC} values found by extrapolation are marked with an asterisk (*).

The J_{SC} for the low laser power densities (1 and 10 W/cm^2, Table 4) shows almost no variation for the different heat sinks proposed. At 10 W/cm^2, comparing the highest heat convection coefficient (10^5 W/m^2·K) with the lowest (250 W/m^2·K) provides a less than 2% reduction of the J_{SC}. The efficiency of the device at these laser power densities is also shown in Table 4. At 1 and 10 W/cm^2, all the efficiencies are within a very near range, implying that at these laser power densities no intricate heat sink technology is needed to ensure a proper functioning of the laser power converter.

Comparing the variation in V_{OC} for those same heat coefficients, we obtain a reduction of a 2.5% at 1 W/cm^2 (from 10^5 to 250 W/m^2·K) and a 7.1% at 10 W/cm^2. However, the reduction in V_M is much less

Table 4
Main figures of merit of the proposed devices at 1 and 10 W/cm^2 using different heat convection coefficients: 10^5, 10^4, $2{\cdot}10^3$ and 250 W/m^2·K. The V_{OC} values marked with an asterisk (*) are found by extrapolating the J-V curves, due to lack of convergence in bias values past V_M.

Pin [W/cm^2]	1				10			
h [W/m^{2}K]	10^5	10^4	$2\cdot10^3$	250	10^5	10^4	$2\cdot10^3$	250
J_{SC} [A/cm^2]	0.258	0.258	0.258	0.256	2.68	2.68	2.67	2.63
V_{OC} [V]	2.83	2.83	2.82	2.76*	2.94	2.93	2.87*	2.73*
V_M [V]	2.65	2.65	2.65	2.64	2.77	2.76	2.76	2.68
T_{VM} [K]	298.0	298.1	298.6	303.1	298.1	299.0	303.1	341.9
Eff [%]	67.4	67.4	67.3	67.1	72.7	72.6	72.4	70.4

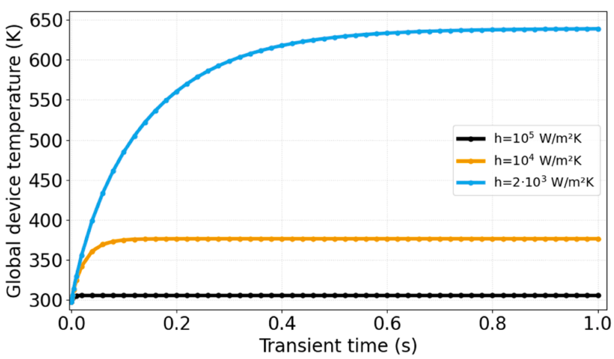

Fig. 6. Global device temperature vs. transient time for the proposed device at a laser power density of 100 W/cm^2 using different heat convection coefficients: 10^5, 10^4 and $2{\cdot}10^3$ W/m^2·K.

pronounced, only a 0.3% at 1 W/cm^2 and a 3.2% at 10 W/cm^2. This can be explained with the temperature at the maximum power point (T_{VM}). For 1 W/cm^2, the T_{VM} is increased by 5.1 K between the highest and the lowest heat convection coefficient scenarios. If we apply the common relation for voltage reduction due to temperature in silicon of ≈2 mV/K [66] to that temperature difference, we obtain 10.2 mV, similar to the difference in V_M observed in Table 4 at 1 W/cm^2. For 10 W/cm^2, the increase of T_{VM} is 43.8 K between the heat convection coefficients of 10^5 and 250 W/m^2·K. Applying the relation of voltage decrease due to temperature produces a voltage shift of 87.6 mV, similar to the V_M TCAD results. This reduction of less than 0.1 V results in a marginal efficiency drop of 2.3%. At these low laser power densities, the heat sink values used in the simulations are enough to maintain a high efficiency. The larger decrease in V_{OC} can be explained through the temperature variations along the J-V curves.

Fig. 7 shows the current density-voltage (left) and the temperature-voltage (right) curves at a laser power density of 1 W/cm^2. The V_M points are marked with a star, while the V_{OC} are marked with a dot, both in the J-V curves and in the T-V curves. The V_M is, as seen before, almost independent of the heat convection coefficient, while the V_{OC} experiences a shift for the smallest h value. This can be explained in the T-V curves, Fig. 7 (right). The T_{VM} values for all heat convection coefficients are in a 5.1 K range, while the range of temperatures for all the V_{OC} values is 37.2 K. This is due to the effect of carrier recombination past V_M, which rapidly increase the temperature of the device, leading to a drop in the current density-voltage curve, shifting the V_{OC}.

The shape of the T-V curves can be explained through the two main heat sources in this device: Joule heat and generation-recombination heat. Fig. 8 (a) shows the Joule heat, the generation-recombination heat and the total heat in the device for each bias point at 1 W/cm^2 when using a heat convection coefficient of 250 W/m^2·K. The generation-recombination heat is almost constant for low bias points (along the plateau zone) until the exponential diode behavior recombines all the carriers, greatly increasing the heat. The Joule heating, on the opposite, is maximum in short circuit current conditions, and is reduced as the bias is applied. This is due to the reduction of the built-in voltage and the depletion zone, which increases free carriers in the P/N junction region and reduces the electric resistivity. Fig. 8 (b) and Fig. 8 (c) show a 2D map of the Joule heat inside the device in short circuit current and in maximum power point, respectively ($V = 0$ and $V = V_M$). The Joule heat (shown in logarithmic scale) is 3 orders of magnitude larger around the P/N junction than in the rest of the device in short circuit current conditions. However, at V_M, Joule heat in the P/N junction is no larger than in the rest of the device. This is related to the reduction of the depletion zone and the subsequent flooding of carriers in that region.

The figures of merit for the high laser power densities (100 and 500 W/cm^2) are shown in Table 5. For 100 W/cm^2, three heat convection coefficients scenarios are studied: 10^5, 10^4 and $2{\cdot}10^3$ W/m^2·K. For 500 W/cm^2, only two cases were considered, 10^5 and 10^4 W/m^2·K, since no convergence was found for lower h values. This is attributed to the extremely high temperatures reached by the device under short-circuit conditions at these laser power densities, exceeding 1000 K. In both cases, two contact resistivity scenarios were considered: 10^{-5} and 10^{-4} Ω /cm^2. The variation of the J_{SC} values both at 100 and 500 W/cm^2 is almost neglectable. The V_{OC} and V_M values degrade when either the heat sink performance worsens (smaller h values) or the contact resistivity increases, except for the V_{OC} at $h = 10^5$ W/m^2·K, where the temperature difference is not enough to significantly affect this J-V parameter. The V_{OC} degradation dependence on contact resistivity is linked to the temperature, and so, to the heat convection coefficient. The efficiencies for 100 W/cm^2 range from 75.1% for $h = 10^5$ W/m^2·K and $\rho_c = 10^{-5}$ Ω/cm^2 to 70.4% for $h = 2{\cdot}10^3$ W/m^2·K and $\rho_c = 10^{-4}$ Ω/cm^2. The reduction in efficiency due to the increase of contact resistance, at the same heat convection coefficient, is around 2% for the three h values. In the case of a laser power density of 500 W/cm^2, both the increase of temperature and series resistance severely degrade the performance of the device. The efficiency at $h = 10^5$ W/m^2·K and $\rho_c = 10^{-5}$ Ω/cm^2 is 70.8%, which is 4.3% less than the same case at 100 W/cm^2. Increasing the contact resistivity to 10^{-4} Ω/cm^2 reduces the efficiency to 60.5%, a 10.3% decrease. Decreasing the performance of the heat sink to $h = 10^4$ W/m^2·K produces a reduction in efficiency down to a 66.2% for $\rho_c = 10^{-5}$ Ω/cm^2 and 55.8% for $\rho_c = 10^{-4}$ Ω/cm^2, respectively. These results highlight the relevance of an adequate heat dissipation mechanism at high laser power densities. Note that the largest efficiency degradation due to temperature increase is 4.6% at 500 W/cm^2, when reducing the heat sink coefficient from $h = 10^5$ to 10^4 W/m^2·K. Further reductions in heat sink performance lead to a rapid temperature rise that severely degrades device performance; these conditions could not be simulated due to convergence limitations of Silvaco under such abrupt thermal changes.

Fig. 9 shows the J-V and T-V curves for 500 W/cm^2. The shift on V_{OC} due to contact resistivity is larger the lower the heat convection coefficient, due to the sharp voltage decrease at low h values on bias points past V_M, as previously explained. This can be seen in the J-V curves at 500 W/cm^2, Fig. 9 (left), where the two curves in the $h = 10^5$ W/m^2·K case achieve the same V_{OC} despite the shift in V_M due to contact resistance (10^{-5} and 10^{-4} Ω /cm^2 produce V_M values of 2.68 and 2.30 V,

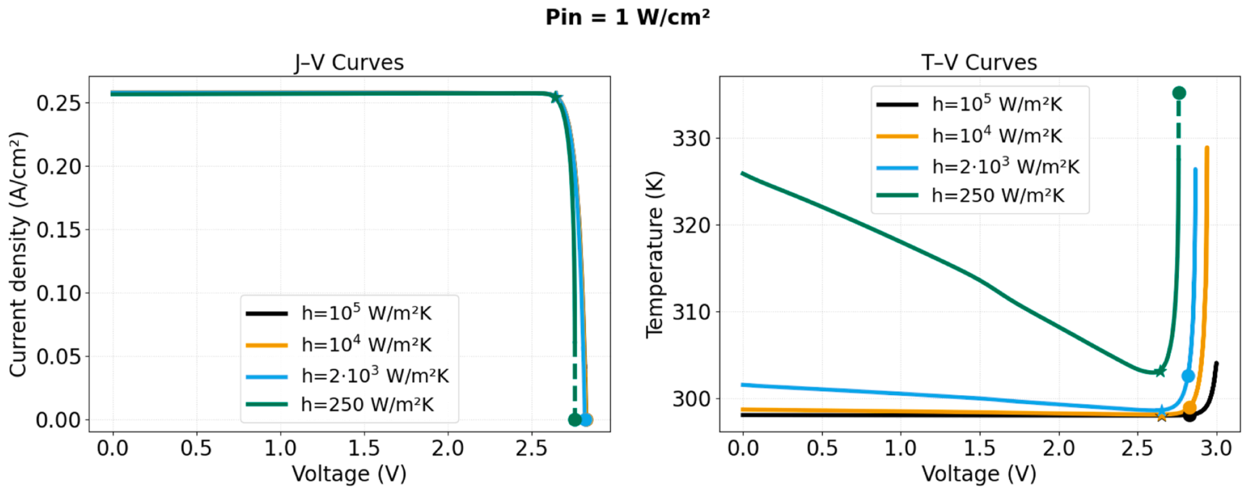

Fig. 7. J-V curves (left) and T-V curves (right) for the 4H-SiC LPC at a laser power density of 1 W/cm^2. The heat convection coefficients considered are h = 10^5, 10^4, 2·10^3 and 250 W/m^2·K.

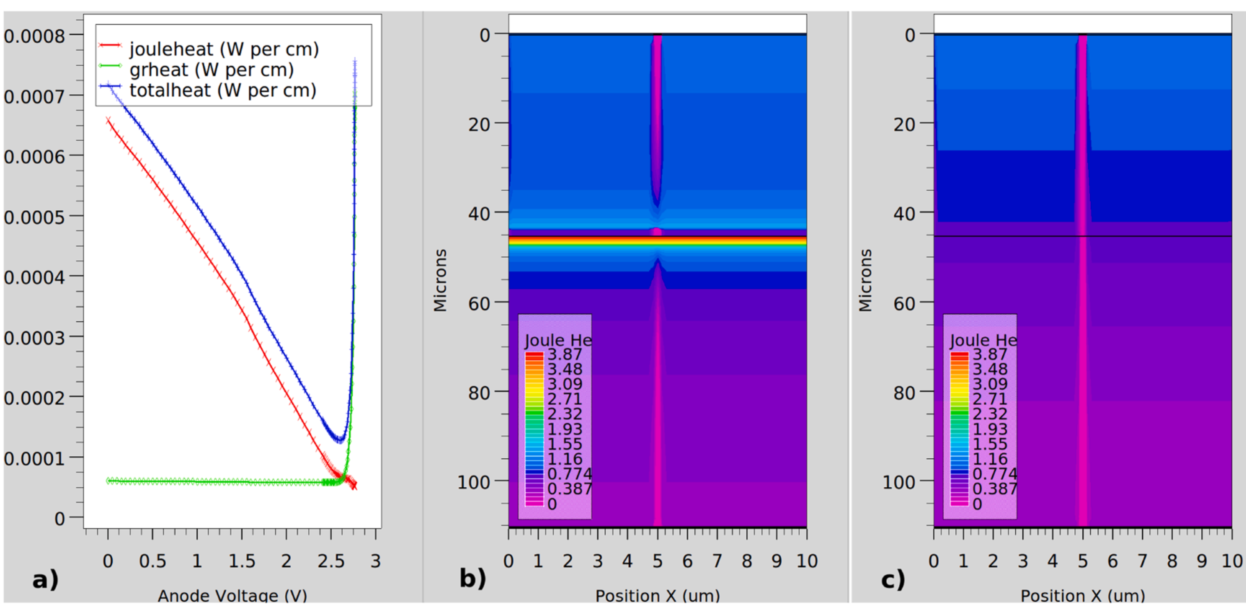

Fig. 8. Integrated Joule, recombination-generation and total heat values of the 4H-SiC device for each bias point (a) and 2D maps of Joule heat (in logarithmic scale) at short circuit current (b) and maximum power point (c) conditions. Units in (a) are divided by the depth of the device. The device is at 1 W/cm^2 and using a heat convection coefficient of 250 W/m^2·K.

Table 5
Main figures of merit of the proposed devices at 100 and 500 W/cm^2 using different heat convection coefficients: 10^5, 10^4 and 2·10^3 W/m^2·K. Two different contact resistivities are considered: 10^{-5} and 10^{-4} Ω/cm^2. No convergence was found for 500 W/cm^2 using a heat sink with h = 2·10^3 W/m^2·K. The V_{OC} values marked with an asterisk (*) are found by extrapolating the J-V curves, due to lack of convergence in bias values past V_M.

Pin [W/cm^2]	100						500			
h [W/m^{2}K]	10^5		10^4		$2 \cdot 10^3$		10^5		10^4	
ρ_c [Ω/cm^2]	10^{-5}	10^{-4}	10^{-5}	10^{-4}	10^{-5}	10^{-4}	10^{-5}	10^{-4}	10^{-5}	10^{-4}
J_{SC} [A/cm^2]	27.08	27.08	27.06	27.06	26.91	26.93	135.77	135.81	135.92	136.25
V_{OC} [V]	2.99	2.99	2.90*	2.88*	2.76*	2.72*	2.98	2.98	2.59*	2.41*
V_M [V]	2.82	2.75	2.81	2.73	2.72	2.64	2.68	2.30	2.50	2.15
T_{VM} [K]	298.9	299.0	307.6	307.5	349.9	349.9	304.5	304.7	377.7	381.1
Eff [%]	75.1	73.0	74.7	72.6	72.5	70.4	70.8	60.5	66.2	55.8

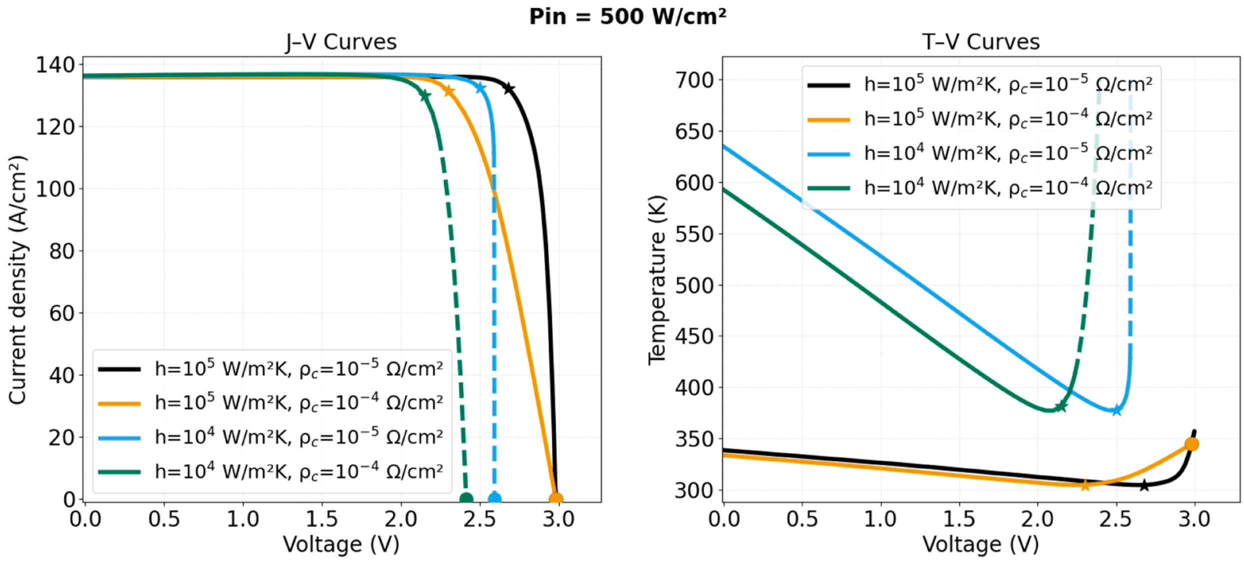

Fig. 9. J-V curves (left) and T-V curves (right) for the 4H-SiC LPC at a laser power density of 500 W/cm^2. The heat convection coefficients considered are h = 10^5 and 10^4 W/m^2·K, and the contact resistivity values are 10^{-5} and 10^{-4} Ω /cm^2.

respectively). However, with a heat convection coefficient of h = 10^4 W/m^2·K, we observe a shift in the V_{OC} value due to contact resistance (2.59 V for 10^{-5}Ω /cm^2 and 2.41 V for 10^{-4}Ω /cm^2), since the large increase in temperature past V_M (see Fig. 9, right) sharply decreases the voltage. The temperature at the maximum power point (T_{VM}) shows almost no dependence with the contact resistivity. As discussed previously, the device temperature at I_{SC} reaches very high values, exceeding 600 K for a heat sink coefficient of h = 10^4 W/m^2·K and ρ_c = 10^{-4} Ω/cm^2. For lower heat sink dissipation values, the temperature rises further, posing convergence challenges for the steady-state numerical solution.

4. Conclusions

In this work, we studied the thermal effects on a novel laser power converter suitable for high power applications, considering all the relevant heat phenomena. For that we implemented a TCAD-based methodology for evaluating the operating temperature of a 4H-SiC LPC and explored the applicability limits of the device for several laser power densities at initial room temperature, considering different heat sink technologies and two scenarios of contact resistivity. All the relevant temperature-dependent models have been included in the simulation framework. The methodology includes: 1) a transient simulation to assess both the steady-state temperature and the time required to reach thermal equilibrium and 2) the steady-state results for each bias point.

The results show that, for low-medium laser power densities (1–10 W/cm^2), the 4H-SiC devices can achieve conversion efficiencies higher than 70% even when using common heat management solutions as forced convection gases, such as a common fin heat sink with a fan. At 1 W/cm^2, the temperature increase between the highest and lowest heat sink dissipation coefficients (10^5 and 250 W/m^2·K) is only 5.1 K, resulting in a negligible efficiency drop of 0.3%. At 10 W/cm^2, this difference grows to 43.8 K, leading to a 2.3% efficiency degradation. In both cases, the impact remains modest, suggesting that simpler, lower-performance heat sink solutions are a viable choice for these power density regimes.

At ultra-high laser power densities (100–500 W/cm^2), higher conversion efficiencies are achievable, but both heat sink performance and contact resistivity become critical design parameters. At 100 W/cm^2, the device achieves a 75.1% efficiency with h = 10^5 W/m^2·K and ρ_c = 10^{-5} Ω/cm^2, while at 500 W/cm^2 the peak efficiency reaches 70.8% under the same conditions. Regarding heat sink performance, reducing the dissipation coefficient from 10^5 to 2·10^3 W/m^2·K at 100 W/cm^2 raises the temperature at the maximum power point by 51 K, resulting in a 2.6% efficiency drop. At 500 W/cm^2, a more moderate reduction to h = 10^4 W/m^2·K already leads to a larger 4.6% efficiency degradation, reflecting the stronger thermal sensitivity at higher power densities. The impact of contact resistivity follows a similar trend. At 100 W/cm^2, increasing ρ_c from 10^{-5} to 10^{-4} Ω/cm^2 produces a ≈2% efficiency reduction, whereas at 500 W/cm^2 the same change leads to a significantly larger degradation of ≈10.4%, for the two h values tested, underscoring the importance of low contact resistivity at ultra-high power densities.

The presented TCAD modeling captures the steady-state thermal behavior of the LPC under a wide range of operating conditions, providing a robust tool for thermal assessment and feasibility evaluation. The transient thermal timescales reported here correspond to the LPC alone, as the heat sink is considered as a global parameter. Future work will explore alternative semiconductor materials as candidates for LPC base substrates, as well as different operating conditions, including initial temperatures relevant to space applications. The effect of heat sinks and thermal interface materials on characteristic transient times can also be explored.

CRediT authorship contribution statement

Javier F. Lozano: Writing – original draft, Software, Investigation, Data curation, Conceptualization; **Natalia Seoane:** Writing – review & editing, Supervision, Funding acquisition, Conceptualization; **Julián G. Fernández:** Writing – review & editing, Investigation; **Enrique Comesaña:** Writing – review & editing, Methodology; **Antonio García-Loureiro:** Writing – review & editing, Project administration, Funding acquisition, Conceptualization.

Declaration of competing interest

The authors declare that they have no known competing financial interests or personal relationships that could have appeared to influence the work reported in this paper.

Data availability

Data will be made available on request.

References

[1] K. Jin, W. Zhou, Wireless laser power transmission: a review of recent progress, IEEE Trans. Power Electron. 34 (2019) 3842–3859.

[2] D. Krut, R. Sudharsanan, W. Nishikawa, T. Isshiki, J. Ermer, N.H. Karam, Monolithic multi-cell GaAs laser power converter with very high current density, Conf. Rec. IEEE Photovolt. Spec. Conf. (2002) 908–911.

[3] C. Algora, I. García, M. Delgado, R. Peña, C. Vázquez, M. Hinojosa, I. Rey-Stolle, Beaming power: photovoltaic laser power converters for power-by-light, Joule 6 (2021) 1–29.

[4] M. Matsuura, H. Nomoto, H. Mamiya, T. Higuchi, D. Masson, S. Fafard, Over 40-W electric power and optical data transmission using an optical fiber, IEEE Trans. Power Electron. 36 (2021) 4532–4539.

[5] H. Helmers, C. Armbruster, M. Von Ravenstein, D. Derix, C. Schoner, 6-W optical power link with integrated optical data transmission, IEEE Trans. Power Electron. 35 (2020) 7904–7909.

[6] C. Vázquez, J.D. López-Cardona, P.C. Lallana, D.S. Montero, F.M.A. Al-Zubaidi, S. Pérez-Prieto, I. Pérez Garcilópez, Multicore fiber scenarios supporting power over fiber in radio over fiber systems, IEEE Access 7 (2019) 158409–158418.

[7] N. Kawashima, K. Takeda, H. Matsuoka, Y. Fujii, M. Yamamoto, Laser energy transmission for a wireless energy supply to robots, in: 22nd International Symposium on Automation and Robotics in Construction, ISARC 2005, International Association for Automation and Robotics in Construction (IAARC), Ferrara, Italy, 2005. https://doi.org/10.22260/ISARC2005/0068.

[8] D. Shi, L. Zhang, H. Ma, Z. Wang, Y. Wang, Z. Cui, Research on wireless power transmission system between satellites, in: 2016 IEEE Wireless Power Transfer Conference, WPTC 2016, 3, IEEE, 2016, pp. 1–4. https://doi.org/10.1109/WPT.2016.7498851.

[9] M. Sanders, J.S. Kang, Utilization of polychromatic laser system for satellite power beaming, IEEE Aerosp. Conf. Proc. (2020) 1–7.

[10] J. Schubert, E. Oliva, F. Dimroth, W. Guter, R. Loeckenhoff, A.W. Bett, High-voltage GaAs photovoltaic laser power converters, IEEE Trans. Electron Devices 56 (2009) 170–175.

[11] S. Fafard, F. Proulx, M.C.A. York, L.S. Richard, P.O. Provost, R. Arès, V. Aimez, D.P. Masson, High-photovoltage GaAs vertical epitaxial monolithic heterostructures with 20 thin p/n junctions and a conversion efficiency of 60%, Appl. Phys. Lett. 109 (2016) 131107.

[12] H. Helmers, E. Lopez, O. Höhn, D. Lackner, J. Schön, M. Schauerte, M. Schachtner, F. Dimroth, A.W. Bett, 68.9% Efficient GaAs-based photonic power conversion enabled by photon recycling and optical resonance, Phys. Status Solidi Rapid Res. Lett. 15 (2021) 1–7.

[13] Y. Gou, Z. Mou, H. Wang, Y. Chen, J. Wang, H. Yang, G. Deng, High-performance laser power converters with resistance to thermal annealing, Opt. Express 32 (2024) 8335–8342.

[14] C. Outes, E.F. Fernandez, N. Seoane, F. Almonacid, A.J. Garcia-Loureiro, GaAs vertical-tunnel-junction converter for ultra-high laser power transfer, IEEE Electron Device Lett. 42 (2021) 1.

[15] N. Seoane, E.F. Fernández, F. Almonacid, A. García-Loureiro, Ultra-efficient intrinsic-vertical-tunnel-junction structures for next-generation concentrator solar cells, Prog. Photovolt.: Res. Appl. 29 (2021) 231–237.

[16] M.C. York, A. Mailhot, A. Boucherif, R. Arès, V. Aimez, S. Fafard, Challenges and strategies for implementing the vertical epitaxial heterostructure architechture (VEHSA) design for concentrated photovoltaic applications, Sol. Energy Mater. Sol. Cells 181 (2018) 46–52.

[17] S. Fafard, D.P. Masson, Perspective on photovoltaic optical power converters, J. Appl. Phys. 130 (2021) 160901.

[18] Y. Gou, H. Wang, J. Wang, Y. Chen, Z. Mou, Y. Chen, H. Yang, G. Deng, High-performance laser power converters for wireless information transmission applications, Opt. Express 31 (2023) 34937–34945.

[19] E.F. Fernández, A. García-Loureiro, N. Seoane, F. Almonacid, Band-gap material selection for remote high-power laser transmission, Sol. Energy Mater. Sol. Cells 235 (2022) 111483.

[20] E. Oliva, F. Dimroth, A.W. Bett, GaAs converters for high power densities of laser illumination, Prog. Photovolt. Res. Appl. 16 (2008) 289–295.

[21] M. Lin, W.E. Sha, W. Zhong, D. Xu, Intrinsic losses in photovoltaic laser power converters, Appl. Phys. Lett. 118 (2021) 1–5.

[22] X. She, A.Q. Huang, O. Lucia, B. Ozpineci, Review of silicon carbide power devices and their applications, IEEE Trans. Ind. Electron. 64 (2017) 8193–8205.

[23] J.N. Shenoy, J.A. Cooper, M.R. Melloch, High-voltage double-implanted power MOSFET's in 6H-SiC, IEEE Electron Device Lett. 18 (1997) 93–95.

[24] J.-M. Lauenstein, M.C. Casey, R.L. Ladbury, H.S. Kim, A.M. Phan, A.D. Topper, Space radiation effects on SiC power device reliability, in: 2021 IEEE International Reliability Physics Symposium (IRPS), IEEE, 2021, pp. 1–8. https://doi.org/10.1109/IRPS46558.2021.9405180.

[25] S. Tudisco, F. La Via, C. Agodi, C. Altana, G. Borghi, M. Boscardin, G. Bussolino, L. Calcagno, M. Camarda, F. Cappuzzello, D. Carbone, S. Cascino, G. Casini, M. Cavallaro, C. Ciampi, G. Cirrone, G. Cuttone, A. Fazzi, D. Giove, G. Gorini, L. Labate, G. Lanzalone, G. Litrico, G. Longo, D. Lo Presti, M. Mauceri, R. Modica, M. Moschetti, A. Muoio, F. Musumeci, G. Pasquali, G. Petringa, N. Piluso, G. Poggi, S. Privitera, S. Puglia, V. Puglisi, M. Rebai, S. Ronchin, A. Santangelo, A. Stefanini, A. Trifirò, M. Zimbone, SiCILIA–silicon carbide detectors for intense luminosity investigations and applications, Sensors 18 (2018) 2289.

[26] R.K. Baruah, B.K. Mahajan, Y.-P. Chen, R.P. Paily, A junctionless silicon carbide transistor for harsh environment applications, J. Electron. Mater. 50 (2021) 5682–5690.

[27] E.J. Brandon, R. Bugga, J. Grandidier, J.L. Hall, J.A. Schwartz, S. Limaye, Power Beaming for Long Life Venus Surface Missions NIAC Phase I Final Report, Technical Report, (2020).

[28] A.E. Arvanitopoulos, M. Antoniou, S. Perkins, M. Jennings, M.B. Guadas, K.N. Gyftakis, N. Lophitis, On the suitability of 3C-Silicon carbide as an alternative to 4H-silicon carbide for power diodes, IEEE Trans. Ind. Appl. 55 (2019) 4080–4090.

[29] I. García, M. Hinojosa, M. Delgado, C. Algora, Photovoltaic laser power converters producing 21 w/cm2 at a conversion efficiency of 66.5%, Cell Rep. Phys. Sci. 5 (2024) 102263.

[30] S.K. Reichmuth, H. Helmers, S.P. Philipps, M. Schachtner, G. Siefer, A.W. Bett, On the temperature dependence of dual-junction laser power converters, Prog. Photovolt. Res. Appl. 25 (2017) 67–75.

[31] M.Z. Shvarts, V.M. Emelyanov, D.A. Malevskiy, M.A. Mintairov, S.A. Mintairov, M.V. Nakhimovich, P.V. Pokrovskiy, R.A. Salii, N.A. Kalyuzhnyy, Temperature tweaking of the output photovoltaic parameters of laser power converters, IEEE Electron Device Lett. 41 (2020) 1324–1327.

[32] J. Yin, Y. Sun, A. Wang, S. Yu, J. Wang, Q. Fu, J. Qin, Y. Han, W. Zhang, S. Zhang, C. Xue, J. Dong, High-voltage 1064 nm ingaasp multijunction laser power converters, IEEE Electron Device Lett. 43 (2022) 1291–1294.

[33] S. Fafard, D.P. Masson, 74.7% Efficient GaAs-based laser power converters at 808 nm at 150 K, Photonics 9 (2022) 579.

[34] S. Fafard, D.P. Masson, 67.5% Efficient InP-based laser power converters at 1470 nm at 77 k, Photonics 11 (2024) 130.

[35] J.F. Geisz, D.J. Friedman, M.A. Steiner, R.M. France, T. Song, Operando temperature measurements of photovoltaic laser power converter devices under continuous high-intensity illumination, IEEE J. Photovolt. 13 (2023) 808–813.

[36] D. Cardwell, Luminescent temperature measurements and thermal resistance characterization of laser power converter photovoltaics, in: 2024 IEEE 52nd Photovoltaic Specialist Conference (PVSC), 2024, pp. 1201–1203. https://doi.org/10.1109/PVSC57443.2024.10748995.

[37] G. Li, C. Wang, N. Zhao, H. Zhang, J. Lu, Numerical simulation of the effect of laser intensity and temperature on the performance of laser power converters, Opt. Eng. 61 (2022) 017103.

[38] J.F. Lozano, N. Seoane, E. Comesaña, F.M. Almonacid, E.F. Fernández, A. García-Loureiro, A new path towards ultra-high efficient laser power converters: silicon carbide-based multijunction devices, Results Eng. 21 (2024) 101987.

[39] Silvaco, Silvaco software (version 5.30.0.R), (2020). https://www.silvaco.com

[40] M. Ochoa, E. Barrigón, L. Barrutia, I. García, I. Rey-Stolle, C. Algora, Limiting factors on the semiconductor structure of III-V multijunction solar cells for ultra-high concentration (1000–5000 suns), Prog. Photovolt. Res. Appl. 24 (2016) 1332–1345.

[41] S. Sze, K.K. Ng, Physics of Semiconductor Devices, John Wiley & Sons, Inc., Hoboken, NJ, USA, (2006), https://doi.org/10.1002/0470068329.

[42] G. Wachutka, Rigorous thermodynamic treatment of heat generation and conduction in semiconductor device modeling, IEEE Trans. Comput. Aided Des. Integr. Circuits Syst. 9 (1990) 1141–1149.

[43] S. Selberherr, Analysis and Simulation of Semiconductor Devices, Springer-Verlag, Vienna, (1984). https://doi.org/10.1007/978-3-7091-8752-4.

[44] B.N. Pushpakaran, S.B. Bayne, Modeling and Electrothermal Simulation of SiC Power Devices, WORLD SCIENTIFIC, (2019), https://doi.org/10.1142/10929.

[45] W.J. Hsiung, C.S. Tan, New debye temperature model of 4h-sic crystal, Phys. Status Solidi 261 (2024) 2400104.

[46] J. Callaway, Model for lattice thermal conductivity at low temperatures, Phys. Rev. 113 (1959) 1046–1051.

[47] J. Ziman, Electrons and Phonons: The Theory of Transport Phenomena in Solids, Oxford University Press, (2001). https://doi.org/10.1093/acprof:oso/9780198507796.001.0001.

[48] Z. Li, H. Lee, C. Wolverton, Y. Xia, High-throughput computational framework for high-order anharmonic thermal transport in cubic and tetragonal crystals, Npj Comput. Mater. 12 (2025) 51.

[49] T. Feng, X. Ruan, Quantum mechanical prediction of four-phonon scattering rates and reduced thermal conductivity of solids, Phys. Rev. B 93 (2016) 045202.

[50] M. Kazan, L. Ottaviani, E. Moussaed, R. Nader, P. Masri, Effect of introducing gettering sites and subsequent au diffusion on the thermal conductivity and the free carrier concentration in n-type 4h-sic, J. Appl. Phys. 103 (2008) 053707.

[51] Y. Varshni, Temperature dependence of the energy gap in semiconductors, Physica 34 (1967) 149–154.

[52] W. Choyke, Optical properties of polytypes of sic: interband absorption, and luminescence of nitrogen-exciton complexes, in: H. Henisch, R. Roy (Eds.), Silicon Carbide–1968, Pergamon, (1969), pp. S141–S152. https://doi.org/10.1016/B978-0-08-006768-1.50018-8.

[53] P. Grivickas, V. Grivickas, J. Linnros, A. Galeckas, Fundamental band edge absorption in nominally undoped and doped 4h–sic, J. Appl. Phys. 101 (2007) 123521.

[54] D.M. Caughey, R.E. Thomas, Carrier mobilities in silicon empirically related to doping and field, Proc. IEEE 55 (1967) 2192–2193.

[55] J. Pernot, W. Zawadzki, S. Contreras, J.L. Robert, E. Neyret, L. Di Cioccio, Electrical transport in n-type 4h silicon carbide, J. Appl. Phys. 90 (2001) 1869–1878.

[56] A. Koizumi, J. Suda, T. Kimoto, Temperature and doping dependencies of electrical properties in al-doped 4h-sic epitaxial layers, J. Appl. Phys. 106 (2009) 013716.

[57] G.L. Harris, Properties of Silicon Carbide, EMIS datareviews series ; no. 13, INSPEC, Institution of Electrical Engineers, London, (1995).

[58] H. Ou, Y. Ou, A. Argyraki, S. Schimmel, M. Kaiser, P. Wellmann, M.K. Linnarsson, V. Jokubavicius, J. Sun, R. Liljedahl, M. Syväjärvi, Advances in wide bandgap SiC for optoelectronics, Eur. Phys. J. B 87 (2014) 58.

[59] E.D. Palik, S. Diego, L. Boston, N. York, S.T. Toronto, Handbook of Optical Constants of Solids, Technical Report, (1998).

[60] M.A. Green, J. Zhao, A. Wang, S.R. Wenham, 45% Efficient silicon photovoltaic cell under monochromatic light, IEEE Electron Device Lett. 13 (1992) 317–318.

[61] D.A. Vartak, Y. Ghotekar, P.M. Bhatt, B. Makwana, H. Shah, J. Vadher, A review: carbon nanotubes composite to enhance thermal & electrical properties for the space applications, Aust. J. Mech. Eng. 22 (2024) 566–574.

[62] F.P. Incropera, D.P. DeWitt, T.L. Bergman, A.S. Lavine, Fundamentals of Heat and Mass Transfer, 6th edition, John Wiley & Sons, Hoboken, NJ, (2007).

[63] Y. Zhang, Y. Yang, X. Chen, B. Liu, X. Yang, Y. Gao, Z. Zhang, D. Kong, D. Lei, Z. Kuai, Z. Li, R. Wang, High-efficiency heat sink design via slm-processed diamond tpms cucrzr alloy: optimizing thermal-fluid performance through volume fraction control, Int. J. Therm. Sci. 223 (2026) 110657.

[64] C. Algora, V. Díaz, Influence of series resistance on guidelines for manufacture of concentrator p-on-n gaas solar cells, Prog. Photovolt. Res. Appl. 8 (2000) 211–225.

[65] A.R. Moore, An optimized grid design for a sun-concentrator solar cell, (1979). https://api.semanticscholar.org/CorpusID:109628879

[66] A.B. Sproul, M.A. Green, Improved value for the silicon intrinsic carrier concentration from 275 to 375 k, J. Appl. Phys. 70 (1991) 846–854.